


## ORIGINAL ARTICLE

# Lognormal Random Field models to identify temporal Land cover changes using full polarimetric L-Band SAR imagery

Welikanna, D. R.<sup>\*a</sup> , Tamura, M.<sup>b</sup>

<sup>a</sup> Department of Surveying and Geodesy, Faculty of Geomatics, Sabaragamuwa University of Sri Lanka, Sri Lanka

<sup>b</sup> Department of Civil and Earth Resources Engineering, Kyoto University, Kyoto, Japan

## ARTICLE INFO

## Article history:

Received 4 March 2021

Received in revised form 29 April 2021

Accepted 30 April 2021

Available online 31 May 2021

## Keywords:

Multiplicative Autoregressive Random Fields (MAR),

Texture,

Variograms,

Structural Similarity Index (SSIM),

Mean Ratio Detector (MRD)

## ABSTRACT

Multiplicative Autoregressive Random Field (MAR) based texture models have been identified as one of the most appropriate models for SAR intensity images to capture the stochastic spatial interaction among neighboring pixels. But very few studies have tested their viability particularly in disaster applications. In this paper, we analyse the MAR texture models for their advantageous in land cover change detection compared to the changes resulting from logarithm of SAR image intensity and speckle filtered SAR imagery. The paper shows that lognormal random fields with multiplicative spatial interactions in the form of MAR models can be an effective alternative to suppress speckle noise and model SAR image intensity in time series data analysis. The pre and post disaster observational data of the Tohoku earthquake, in the east coast of Japan, acquired by the Advanced Land Observation Satellite (ALOS)/phased array type L-band synthetic aperture radar (PALSAR) were synthesized using MAR model based texture measures. Two of the main texture descriptors of the MAR model were considered primarily in this study. Those are the neighborhood weighting and the noise variance parameters. A 2<sup>nd</sup> order neighborhood configuration was used to estimate them. We present a variogram based analysis, structural similarity index measure (SSIM), and the mean ratio detector (MRD) as three different approaches to analyse the changes in land cover using radar texture. The change detection results of the MRD were further tested using area error proportion (AEP), root mean square error (RMSE) and correlation coefficient (CC), keeping normalized ratio, principle component analysis (PCA) and adaptive Lee filtered polarimetric intensity based change as the references.

## 1 Introduction

Monitoring structural changes of land cover due to different magnitudes of disasters is an important usage of the earth orbiting SAR imagery. This advantage of the SAR over its optical counterpart is made possible by the capabilities of acquiring all weather, cloud insensitive multi-date digital imagery at a global scale. Backscatter intensity, texture descriptors and interferometric coherence are the primary image features embedded in both amplitude and phase of the recorded scattered wave of the SAR sensor available for change analysis (Del Frate et

al., 2008). Due to the coherent nature of the illumination, radar image pixels are subjected to the effect of speckle noise. Attempts to reduce speckle by coherent spatial averaging, which reduces both fading and spatial resolution, have met with limited success in feature extraction (Ulaby et al., 1986). Speckle as a random effect minimizes the optimal use of SAR pixels for the pre and post disaster comparison in the case of change detection. As a result, SAR image pixel values become unreliable in the interpretation of spatial patterns. Hence it is useful and appealing to investigate the possibilities of extracting the spatial patterns of backscatters using textural operators (Del Frate et al., 2008). Texture features reflect the structural arrangement of the ground objects, with strong relationship to their changes. Temporal changes to the state of land cover can happen due to natural and manmade effects. Two kinds of changes can be considered primarily, abrupt changes corresponding to strong modifications to the state of land cover and the smooth transitions corresponding to slow evolutions (Bujor et al.,

\* Corresponding author: Department of Surveying and Geodesy, Sabaragamuwa University of Sri Lanka, Sri Lanka.

E-mail address: [drw@geo.sab.ac.lk](mailto:drw@geo.sab.ac.lk) [dumindarw@gmail.com](mailto:dumindarw@gmail.com) (D.R. Welikanna).



2004). Due to earthquakes and tsunami effects, changes to the state of stable land cover can occur mainly in the form of building collapses and debris in urban and barren landscapes, as well as inundations in agricultural lands and areas surrounding lagoons.

Spatial configuration in a coastal urban area is a combination of heterogeneous land cover components such as vegetation, impervious surface and soil. The inherent nature of the spatial discontinuity of these features makes it difficult to detect them from a single SAR image due to the effect of speckle noise. Hence multitemporal SAR data can be useful to minimize the speckle and extract the variations. Modelling spatial correlation in radar images, using independent and identically distributed models can be considered as an over simplification of a complex process. Transforming the data to Gaussian statistics and modelling them with linear spatial interactions can be more effective in such instances. Lognormal random field models with multiplicative spatial interactions are a special case of a transformed Gaussian random field for SAR images. Multiplicative autoregressive random fields (MAR), which is a 2-D lognormal random field, is employed in this study to synthesize the radar images into textures. The parameters of a MAR model are highly correlated with spatial distribution corresponding to the intrinsic variability of the backscattering coefficients (Dierking and Skriver, 2002). Furthermore MAR model based texture for radar images become more appealing due to the ability to model both the spatial correlation structure and the distribution of the grey-levels (Dierking and Skriver, 2002).

Different SAR image change detection algorithms were developed and tested for many years (Bruzzone and Prieto, 2000; Chellappa and Chatterjee, 1985; Cross and Jain, 1983; Del Frate et al., 2008; Ehrlich et al., 2009; Gamba et al., 2006; Solberg and Jain, 1997). Among them, the methods based on texture feature have received more attention, mainly because they can suppress the effect of SAR image speckle noise (Bujor et al., 2004; Dekker, 2003; Gamba and Aldrighi, 2012; Stasolla and Gamba, 2008). It was also observed that radar speckle has a standard deviation linearly related to the pixel mean values and are often modelled as a multiplicative process (Qiu et al., 2004). On the context of texture, the first order statistics of the fading random variables describe their probability density functions while the second order fading texture statistics, such as the auto correlation function, describe the relationship between pixels and its neighbors (Ulaby et al., 1986). A comprehensive discussion of the properties of second order statistics, which describes how often one gray tone will appear in a specific spatial relationship to another gray tone, can be found in (Haralick et al., 1973; Ulaby et al., 1986). Lognormal Random field based radar image synthesis was first proposed by Franknote and Chellappa (1987) in detail. MAR model based texture parameters using RADARSAT data were employed in one of the studies to detect forest fires, as a major application (Park et al., 2001). Here it was summarized that the fusion of textural information with the information such as changes in backscatter can improve the results. As a whole, very few

efforts were carried out to use the MAR based texture for spatiotemporal changes.

In this study, an investigation is made to analyse the feasibility of MAR based texture parameters to extract temporal changes in an earthquake and tsunami context. These findings are reported as an alternative means to extract changes independent of the polarimetric techniques tested extensively for such purposes.

## 2 Data Description and Pre-Processing

The region of focus for the study covers the heavily damaged Ishinomaki and Onagawa areas from the 2011 Tohoku Earthquake and Tsunami. Ishinomaki city and the areas north to the city are located in a flat basin. Two main rivers flow through the area, where one runs to the south through Ishinomaki city (Old-Kitakami river), while the other runs eastward through Ogatsu area (Kitakami river). Many of the primary land covers of the area belong to cultivated paddy lands while impervious, soil and vegetation dominate the rest. A post disaster Advanced Visible and Near-Infrared Radiometer-2 (AVNIR-2) acquired on 10<sup>th</sup> April 2011 and Google earth pre and post disaster images of 25<sup>th</sup> June 2011 and 12<sup>th</sup> March 2011 were also employed for the results validation. A combination of pre and post disaster Advance Land Observation Satellite (ALOS) phased array type L-band synthetic aperture radar (PALSAR) data set was used in this study. This is a dataset resulted from an urgent data acquisition after the earthquake on 11<sup>th</sup> March 2011. Full polarimetric observation conducted on 8<sup>th</sup> April 2011 was taken as the post-disaster data set, while the observation made on 21<sup>st</sup> November 2010 was the pre-disaster input. Observation mode was an off-nadir angle of 21.5° in the ascending orbit. A single look PolSAR image carries a resolution of 4.45m in azimuth and 23.14m in ground range direction. The revisit cycle for ALOS is 46 days. The temporal base line is 138 days and the perpendicular base line is about 2km. Such a large temporal and spatial baseline can induce significant decorrelation effects and produce poor interferometric coherence. The PALSAR images were geocoded using UTM projection (zone 54N) and WGS84 Datum. Multilooking (5-look) processing in azimuth direction was performed to adjust the azimuth and range pixel size to be comparable, with a resulting spatial resolution of 25m. No speckle filters were applied initially on the data in the case of MAR based texture generation. At the same time, we used an adoptive Lee filter to suppress the speckle effects using the SAR intensity and performed a log transformation to compare the texture based changes and the changes resulting from despeckling. Adaptive Lee filter assumes that mean and the variance of a pixel in focus are equal to the local mean and the variance of all pixels within the user defined moving window. A 3 × 3 pixel moving window was used for the filtering process. From among the most commonly used adaptive filters, the choice of the Lee filter in the study is because of its superiority to preserve prominent edges, linear features, point targets, and texture information (Qiu et al., 2004).

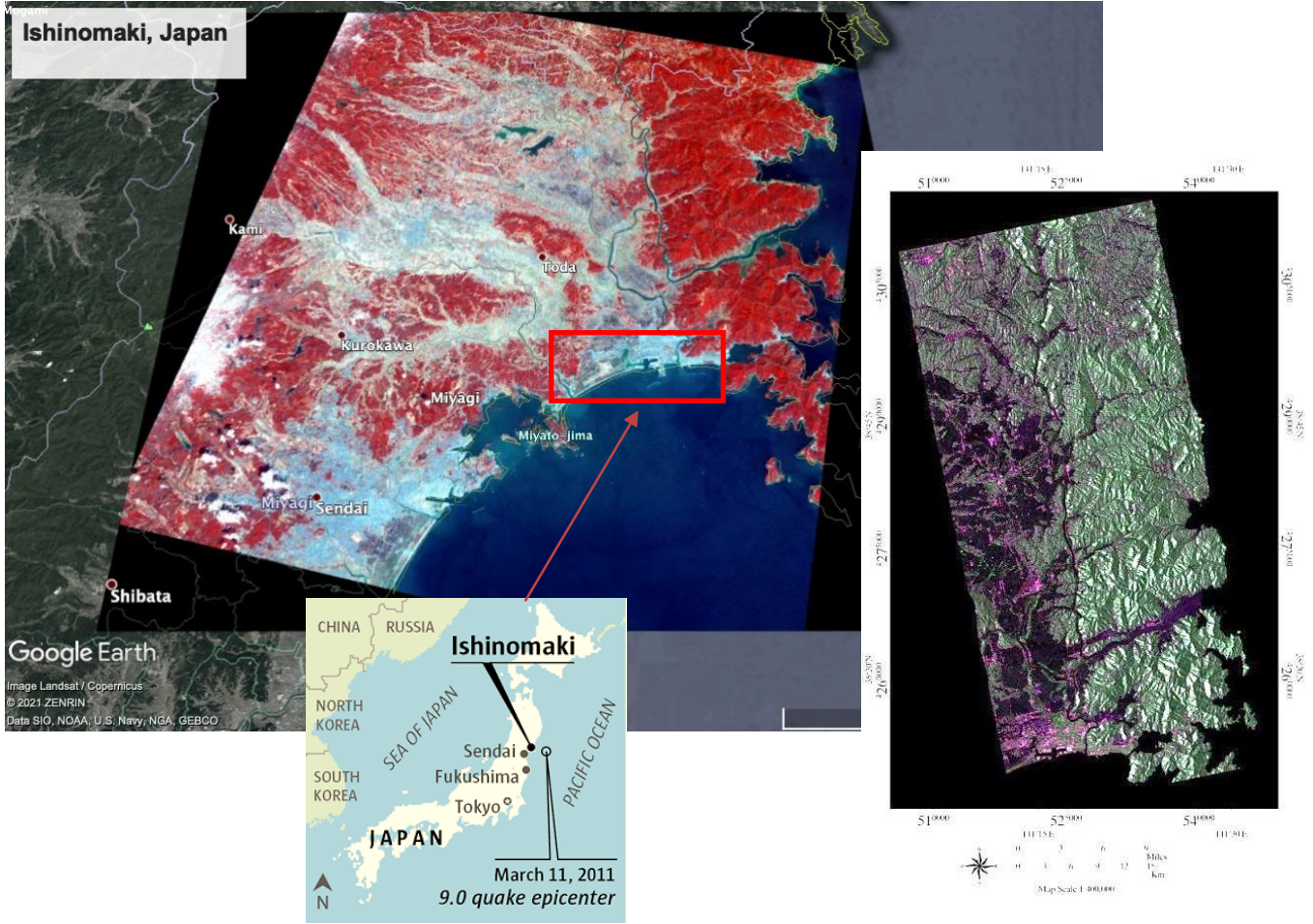


**Fig. 1:** Study area map with earthquake epicentre (source-USGS) and the pre disaster AVNIR-2 false colour composite, AVNIR ALOS PALSAR 5-look complex images with HH, VH and VV polarization components in RGB, respectively, for the post disaster scene on 8<sup>th</sup> April 2011.

The study area map and the 5-look intensity post disaster PALSAR image is shown in Fig.1.

### 3 MAR based texture and change detection methods

In this section, we discuss the MAR based texture synthesis and change detection methods. Firstly, Semivariograms, which represent the spatial dependence of each pixel to its neighbors, were used to identify the changes in the pre and post disaster texture components. Secondly, we test the structural similarity index (SSIM), which is a very recent measure of the structural similarity between time series images. Finally, we use the mean ratio detector (MRD) measure, which is a standard change detection approach operating in a given spatial neighborhood, to find the contextual dissimilarities using the ratio of the local means.

#### 3.1 MAR model based texture

Let an image  $y(i,j)$  be represented as a random disturbance (noise) driven multiplicative system as in Eq.1:

$$y(i,j) = \prod_{[r=(m,n)] \in N} y(i+m, j+n)^{\theta_r} v(i,j) \quad (1)$$

where  $N$  is the neighborhood set defining the model support,  $v(i,j)$  is the log normal white noise process which is also referred to as the driving process, and  $\theta_r$  is the exponent weighting factor for a neighborhood  $r$ . In the case of first-order neighborhood (Mather and Tso, 2016), four particular neighbors contribute to the centre pixel  $(i,j)$ . Then the centre pixel  $y(i,j)$  can be modelled as:

$$y(i,j) = y(i-1,j)^{\theta_{-1,0}} \times y(i-1,j)^{\theta_{0,-1}} \times y(i-1,j)^{\theta_{1,0}} \times y(i-1,j)^{\theta_{0,1}} \quad (2)$$

Eq.2 was extended for a second order neighborhood configuration in this study. The random field  $y(i,j)$  is said to obey a log-normal MAR model if  $x(i,j) = \ln(y(i,j))$  with  $u(i,j) = \ln(v(i,j))$  obeys a Gaussian autoregressive random field model represented by a difference equation in the form of:

$$x(i,j) = \sum_{[r=(m,n)] \in N} \theta_r x(i+m, j+n) + u(i,j) \quad (3)$$

where  $\theta$  is called the neighborhood weighting parameter and  $u(i,j)$  is the zero mean white Gaussian noise, with the covariance given by:



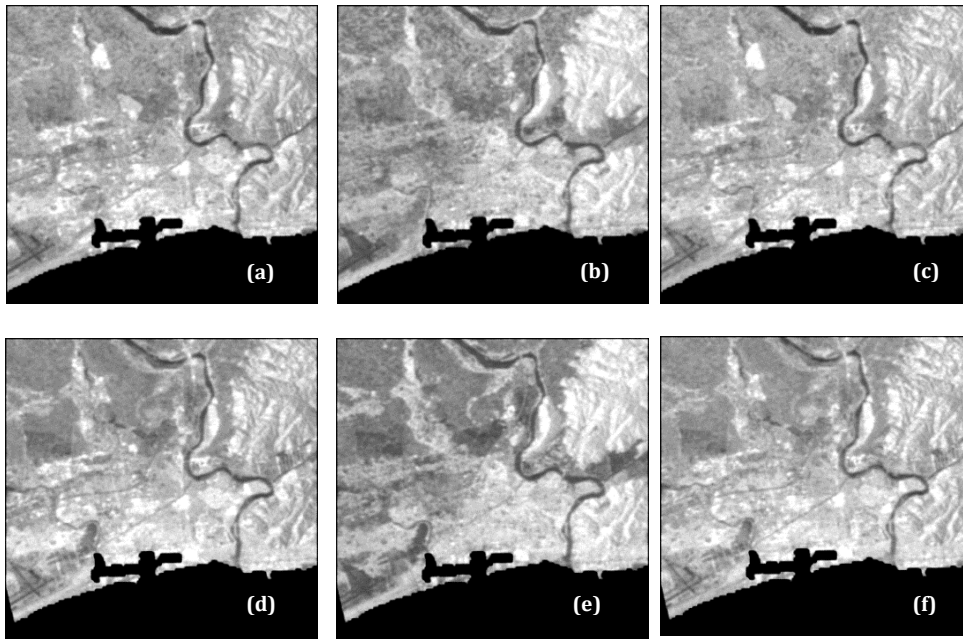


**Fig. 2:** Noise Variance ( $\sigma_u^2$ ) parameter based texture images generated (a), (b), (c) pre disaster (d), (e), (f) post-disaster log estimates of HH,HV,VV polarization.

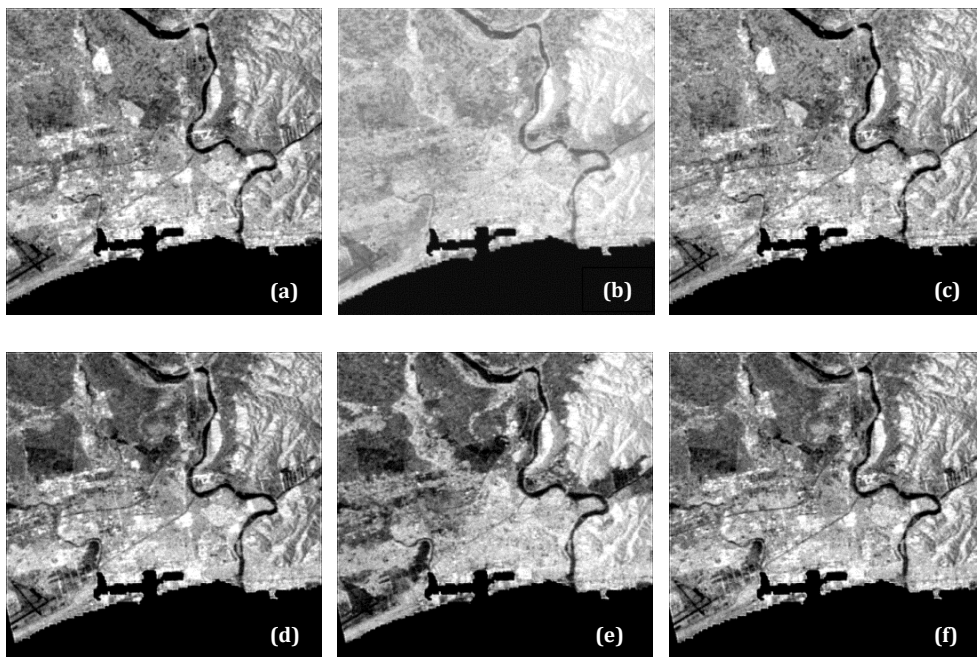


**Fig. 3:** Neighborhood Weight (mean of the parameter  $\theta$  for 2<sup>nd</sup> order neighborhood) parameter based texture images generated (a), (b), (c) pre disaster (d), (e), (f) post-disaster log estimates of HH,HV,VV polarization.

$$Cov_u(r) = \begin{cases} \sigma_u^2, & r = (0,0) \\ 0, & r \neq (0,0) \end{cases} \quad (4)$$

where  $\sigma_u$  is the variance of  $u$ . Three main parameters of the MAR model can be used as texture descriptors. They are; the weighting parameter  $\theta$ , the noise variance  $\sigma_u^2$ , and the mean value  $\delta_x$  of the stationary random process  $x$ . The neighborhood weighting parameter and the noise variance fit the logarithm of the observed data into a Gaussian random field model. The weighting parameter is

nonnegative and explains the degree of possible interaction of the neighborhood pixel values to the pixel in concern (Ord, 1975). The random noise term as explained earlier is uncorrelated, and is normally distributed with zero means and equal variance. These parameters which characterize the image are estimated using the least square estimation with a given image  $y(i,j)$  of size  $M \times M$  and its log transform  $x(i,j) = \ln(y(i,j))$ . They are shown as below:

$$\delta_x = \frac{1}{M^2} \sum_{i,j} x(i,j) \quad (5)$$

$$z(i,j) = x(i+m, j+n) - \delta_x, r \in N \quad (6)$$

$$\sigma_u^2 = \frac{1}{M^2} \sum_{i,j} [x(i,j) - \delta_x - \theta^T \times z(i,j)] \quad (7)$$

$$\theta = \frac{\sum_{i,j} z(i,j) \times (x(i,j) - \delta_x)}{\sum_{i,j} z(i,j) \times z^T(i,j)} \quad (8)$$

In the above equations,  $T$  denotes the transpose of the matrix. Depending on the land surface structure represented in different images, texture parameters will have different values. Hence the images with pixel values defined by each of these parameters can be considered as the synthetic representation of their original images.

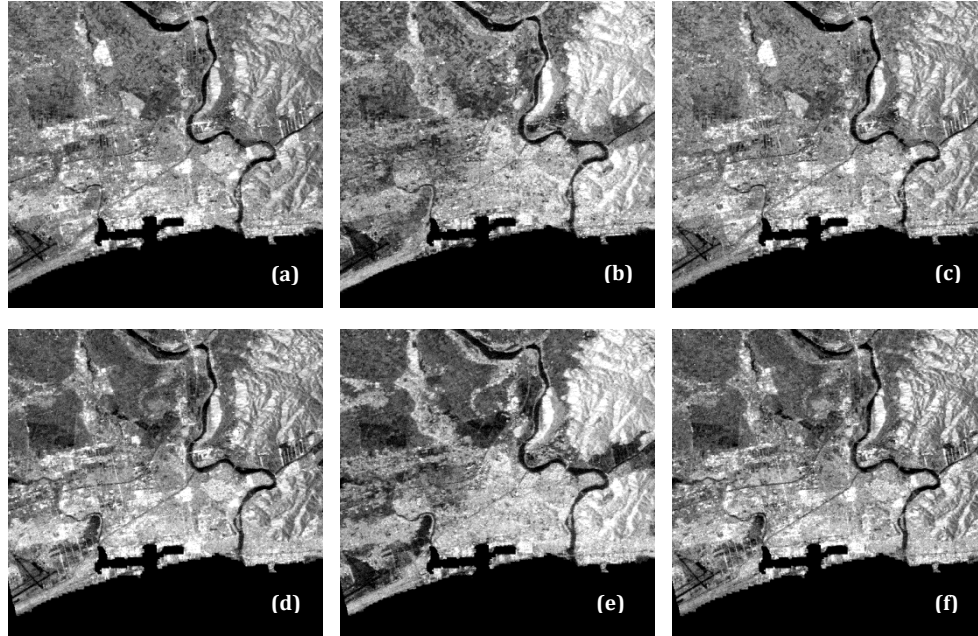


**Fig. 4:** log transformed filtered intensity images (using an adaptive Lee filter) showing the speckle suppression for (a), (b), (c) pre disaster and (d), (e), (f) post-disaster, HH, HV, VV polarization, respectively.

Theoretically, any image processing operation that works on the original image can be performed using these texture parameters. In the current study, we employed two of these three parameters, the neighborhood weighting parameter  $\theta$  and the noise variance  $\sigma_u^2$ . The MAR texture image subsets generated using the above equations are shown for the pre and the post disaster scenes in Fig. 2 and Fig. 3 respectively. In second order statistics resulting from MAR models, the gray tones close to the white represent pixels with strong relation to each other while black gray tones shows regions with isolated entities. The log transformed adaptive Lee filtered pre and post disaster images are shown in Fig. 4, with reduced granular appearance. The log transformation was performed to convert the Gamma distributed pixel intensity into Gaussian distribution for the effective use of the change detection techniques employed in the study. These are the main data inputs for the change detection presented in the study. For impervious surface, paddy and vegetation class samples, Fig. 4 shows Neighborhood Weight ( $\theta$ ) parameter based radar texture difference in pre and post disaster HH and HV polarizations. The approximations of the histograms using a Gaussian fit for each of these samples are shown in the Fig. 5 and Fig. 6. As illustrated by the histograms, the distribution of the texture measures for the SAR intensity can be modelled by Gaussian distribution. A shift in the mean values and the changes in the variance from the pre to the post disaster land cover can be observed from the

histograms. This is mainly due to the changes in the geometric nature and the moisture content (due to sea water of the tsunami) of the disaster affected urban area (Richards, 2009). This also provides the possibility of using MRD conveniently as the changes can be captured by the local mean values of the MAR based texture in a Gaussian framework.

### 3.2 Semivariogram calculation

Both the log transformed radar image pixel values and their texture descriptors are associated with ground locations. Hence, these random variables can be considered as regionalized variables with their known position in space. Thus, it is possible to use variograms to investigate the spatial structure of the urban landscape represented by both the log normal and the MAR model based texture variables of the SAR images. Variograms measure the spatial variation in these regionalized variables (Curran, 1988; Woodcock et al., 1988). Semivariogram function relates semivariance to spatial separation and provides a concise and unbiased description of the scale and pattern of the spatial variability. Therefore, variograms estimate the average value of the pixels belonging to a particular land cover class within a specific region. Both remotely sensed and ground data can be used as samples to construct semivariograms.

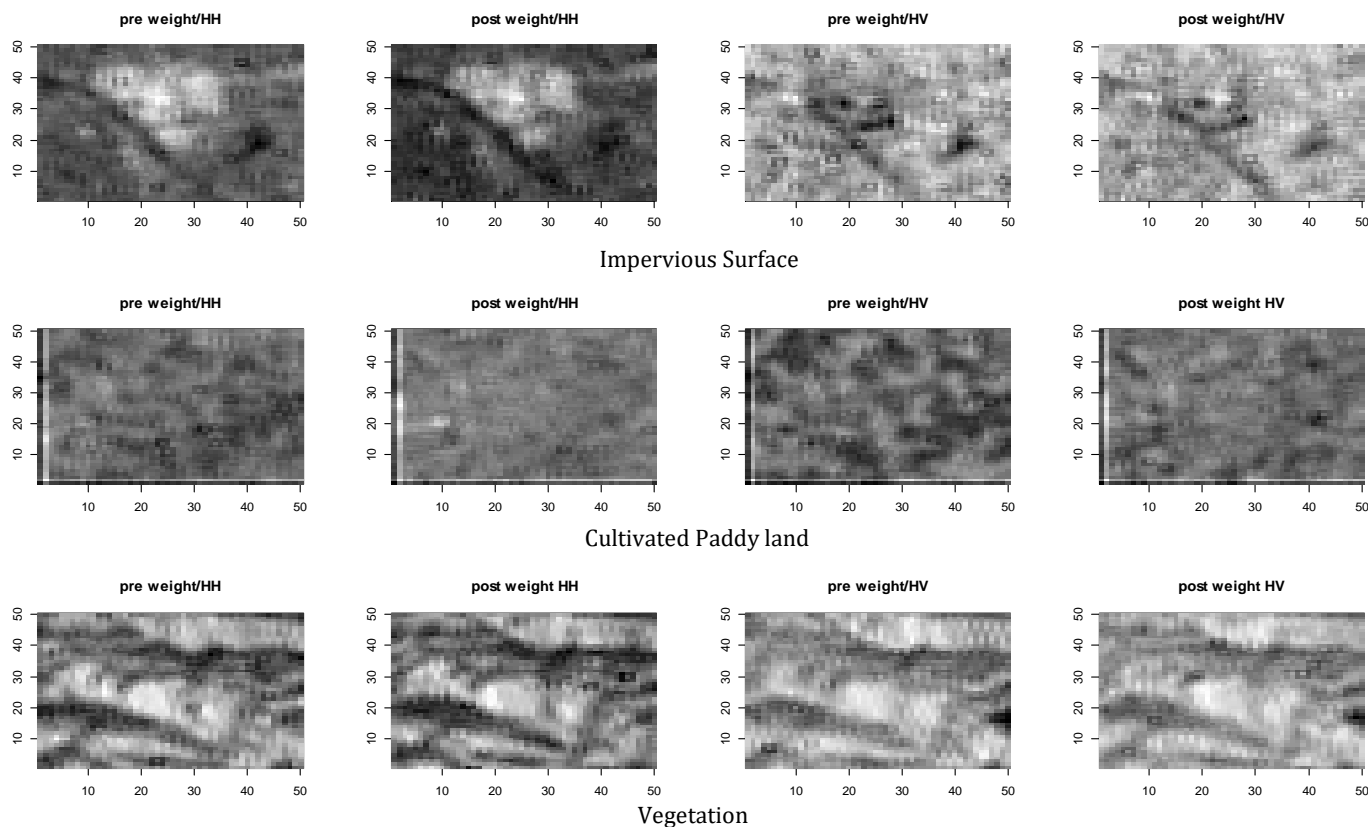


**Fig. 5:** Difference in Neighborhood Weight ( $\theta$ ) parameter based radar texture from pre to post disaster situations in HH and HV polarization, for Impervious surface, Paddy and Vegetation class samples.

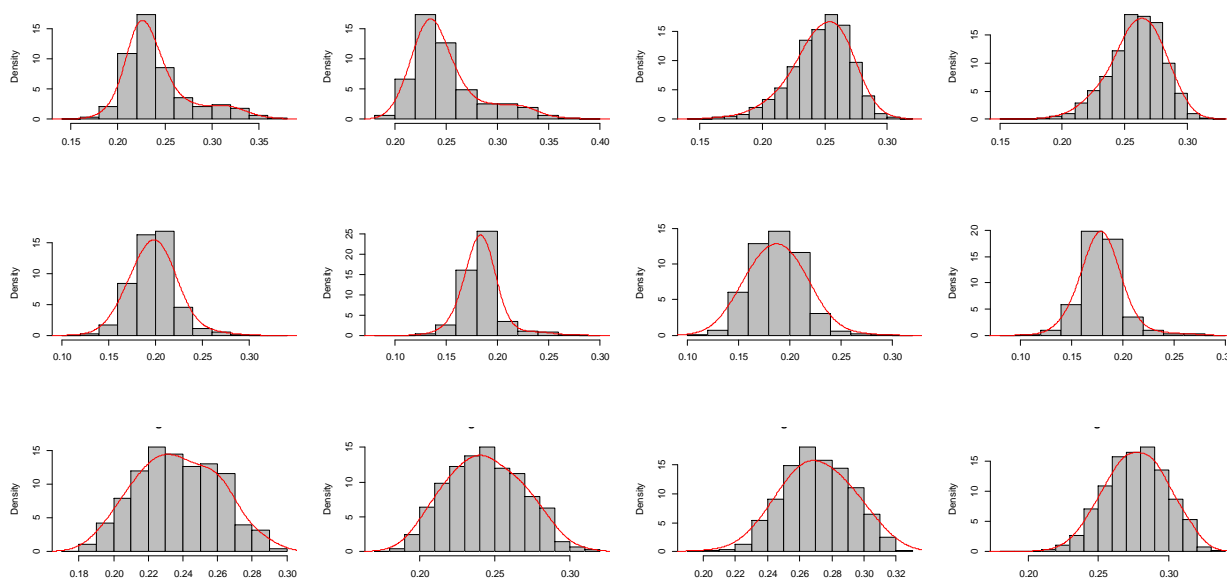


**Fig. 6:** Pixel distribution and Gaussian fit for the class samples shown in Fig. 2 for Neighborhood Weight ( $\theta$  for 2<sup>nd</sup> order neighborhood) parameter based texture image, showing the shift in mean before and after the disaster.

The sensitivity of variograms to multiple scales of variation in images is an important feature for them to be used in disaster change analysis studies. According to Woodcock (Woodcock et al., 1988) the height, also known as sill of the variogram, is related to the density or proportion of the area covered by objects such as buildings or roads. The

distance to sill, or the range of influence, is related to the size of these objects. The shape of the variogram and the range are more sensitive to the area of objects. Furthermore, the shape is also related to the variance of the size of the objects. Hence a change in the objects in a case of a disaster can have significant influence to the shape and

height of the variograms. If the texture based approach is to provide better estimation of the damage from the images, it is necessary that the synthesis preserves the original spatial structure at both pre and post stages of the disaster. We implemented the variograms to investigate further in to the spatial configuration of the image pixel values for the built up area. The calculation of the semivariogram is presented as below:

If a transect of pixels  $M$ , on top of a particular land cover class of interest, is selected from the log transformed, speckle filtered SAR images or the texture image, given its digital number  $x$  at pixel position  $i$  ( $i=1,2,\dots,M$ ), the relationship between a pair of pixels at a lag distance  $h$  can be defined using the average variances of the differences between all such pairs. With the single pixel variance being half of all such combinations, semivariance  $s^2$  for a lag distance of  $h$  can be given by:

$$\gamma^2 = \frac{1}{2}[x(i) - x(i + h)]^2 \quad (9)$$

For a transect or a subset of  $M$  pixels in a particular land cover class with a predefined lag distance, an unbiased estimation of the average semivariance in  $m$  pairs can be defined as follows:

$$S^2 = \frac{1}{2m} \sum_i^m [x(i) - x(i + h)]^2 \quad (10)$$

Effects of natural disasters are directional independent in many of the instances. However, it is useful to model the variograms to suit the presence or absence of the isotropy. In this paper we compute the variograms along a transect, taking into account different directions using a radius defined by  $N$  number of pixels. For  $i=1,2,\dots,M$  and  $j=1,2,\dots,N$  on a regular lattice ( $M \times N$ ), the sample semi-variogram at lag  $(h, k)$  then becomes:

$$g(h, k) = \frac{1}{2(m-h)(n-k)} \sum_i^m \sum_j^n \{ [x(i, j) - x(i + h, j + k)]^2 \} \quad (11)$$

### 3.3 Structural Similarity Index Measure (SSIM)

SSIM is a very recent objective image quality measure used for image quality evaluation. The application of these measures to extract the temporal changes from SAR texture images is very recent and new. The general formula for the SSIM in the case of pre and post disaster MAR weighting parameter based texture is as follows:

$$SSIM = [l(\theta_{pre}, \theta_{post})]^\alpha \cdot [c(\theta_{pre}, \theta_{post})]^\beta \cdot [s(\theta_{pre}, \theta_{post})]^\gamma \quad (12)$$

where,

$$\left. \begin{aligned} l(\theta_{pre}, \theta_{post}) &= \frac{2\mu_{\theta_{pre}}\mu_{\theta_{post}} + c_1}{\mu_{\theta_{pre}}^2 + \mu_{\theta_{post}}^2 + c_1} \\ c(\theta_{pre}, \theta_{post}) &= \frac{2\sigma_{\theta_{pre}}\sigma_{\theta_{post}} + c_2}{\sigma_{\theta_{pre}}^2 + \sigma_{\theta_{post}}^2 + c_2} \\ s(\theta_{pre}, \theta_{post}) &= \frac{2\sigma_{\theta_{pre}\theta_{post}} + c_3}{\sigma_{\theta_{pre}}\sigma_{\theta_{post}} + c_3} \end{aligned} \right\} \quad (13)$$

$\theta_{pre}, \theta_{post}$  are the weighting texture measures generated using MAR models for the pre and post disaster log transformed images ( $x(i, j)$ ) respectively. The first term in Eq.13 is the luminance comparison function, which measures the closeness of the mean luminance of the pre and the post textural images. The second term, which is the contrast comparison function, measures the closeness of the contrast between the two images. Contrast is defined as the standard deviation of the two images ( $\sigma_{\theta_{pre}}, \sigma_{\theta_{post}}$ ). The third is the structure comparison function, where  $\sigma_{\theta_{pre}\theta_{post}}$  is the covariance between the images. This third element relates to the correlation coefficient between the resulting image and the reference. The positive constants  $c_1, c_2$  and  $c_3$  avoid the null denominator. A simplified version of the SSIM results as below (Wang et al., 2004):

$$SSIM(\theta_{pre}, \theta_{post}) = \frac{(2\mu_{\theta_{pre}}\mu_{\theta_{post}})(2\sigma_{\theta_{pre}\theta_{post}})}{(\mu_{\theta_{pre}}^2 + \mu_{\theta_{post}}^2 + c_1)(\sigma_{\theta_{pre}}^2 + \sigma_{\theta_{post}}^2 + c_2)} \quad (14)$$

The  $c_1$  and  $c_2$  parameters were set to take two small contestant values of 0.01 and 0.03 respectively, for more stability in the measurement (Wang et al., 2004). A value 0 for SSIM shows no correlation among the images, while a value 1 suggests that the images are almost similar. Hence the resulting SSIM maps will correspond to dark tones in the areas where spatial changes result. The use of SSIM index with texture for the temporal changes is a novel approach proposed and tested in this study.

### 3.4 Mean Ratio Detector

MRD assumes the changes to occur as a modification of the local mean values in a particular spatial neighborhood of the two images (Inglada and Mercier, 2007). Eq. (15) defines the MRD. The spatial neighborhood considered for this measure was tested from a pixel combination of  $3 \times 3, 5 \times 5$  to  $7 \times 7$ . The effect of these neighborhood configurations for the results were found to be very close; hence the results reported in this study are from a neighborhood size of  $3 \times 3$ .

$$r_{MRD} = 1 - \min \left\{ \frac{\mu_{Nx(t1)}}{\mu_{Nx(t2)}}, \frac{\mu_{Nx(t2)}}{\mu_{Nx(t1)}} \right\} \quad (15)$$

where  $\mu_N$  is the mean value determined for an  $N^{th}$  order spatial neighborhood of the log transformed image  $x$ . MRD based changes were determined for the log estimation as well as the MAR based texture.

### 3.5 Error measure

In addition to the three main approaches for the temporal changes we implemented two fundamental and well known change detection methods to extract the damage areas as our references. They are the image ratio and the principal component transformation (PCA). A normalized ratio measure is attained as shown in Eq. (16) by using the two log transformed images:

$$R(T) = \frac{x(t_1) - x(t_2)}{x(t_1) + x(t_2)} \quad (16)$$

where  $R(T)$  is the ratio of the log transformed images  $x(t_1)$  pixel  $i, j$  at time  $t_1$ . If the log estimation for a pixel of the two images is nearly the same, then  $R(T)$  will take a value close to zero indicating no change, while for a change this will be a larger value (Singh, 1990). In the case of principal component (PC) transformation, the original data are mapped to a new set where the covariance matrix is diagonal so that the data can be represented without correlation. This analysis is made possible because the unchanged areas have high correlation between the pre and post disaster images with common variance for the two days. Further, this can be explained using the first PC that accounts for the maximum possible variance in time series images. Contrarily, changed areas which occupy a small region in the two images would be present in the second principle component. For this purpose, the pre and post disaster images are stacked to perform as a single image, and this combined image is transformed to its PC's. If the stacked image is  $x_s$  with a dimension of  $l = 1, \dots, L$  mathematically as a set  $x_{s_l}^T = [x_{s_1}, x_{s_2}, \dots, x_{s_L}]$ , with the covariance matrix being  $\Sigma$ , the principle component  $sp_l$  of the set can be expressed by the Eq. (17):

$$p_l = e_{l1}x_{s_1} + e_{l2}x_{s_2} + \dots + e_{lL}x_{s_L} \quad (17)$$

$e_l^T = [e_{l1}, \dots, e_{lL}]$  is the eigenvectors of the covariance matrix  $\Sigma$ . There will be high correlation between the two images for the unchanged area while in the case of changes, it will be low (Liu et al., 2004)(Liu et al., 2004)(Liu et al., 2004)(Liu et al., 2004)(Liu et al., 2004)(Liu et al., 2004)(Liu et al., 2004). In this work, we used the log transformed polarimetric components as the input for the PCA based change analysis.

The comparison of the change detection results is a difficult task when considering the problems of the co-registration between the data sets as well as the lack of reliable ground truth information. We compare the change and the no change class area proportions for fixed neighborhood in each of the method using three error measures, root mean square error (RMSE), correlation coefficient (CC) and the area error proportion (AEP) as mentioned in Eq. (18), (19) and (20). After carefully reviewing the damaged area using the available Google historical images and the post disaster AVNIR-2 image, we tried to compare the damages within a 100m×100m area.

$$RMSE = \sqrt{\frac{1}{MN} \sum_i t_{\alpha i}^1 - t_{\alpha i}^2} \quad (18)$$

$$CC_{\alpha} = \frac{\sum_i (\bar{t}_{\alpha}^1 - t_{\alpha i}^1) \cdot (\bar{t}_{\alpha}^2 - t_{\alpha i}^2)}{(M \cdot N - 1) \cdot s_{t_{\alpha}^1} \cdot s_{t_{\alpha}^2}} \quad (19)$$

$$AEP_{\alpha} = \frac{\sum_i (t_{\alpha i}^1 - t_{\alpha i}^2)}{M \cdot N} \quad (20)$$

Here  $t_{\alpha i}^1, t_{\alpha i}^2$  are the fractional estimations of the damaged class  $\alpha$  within a user determined neighborhood of an  $M \times N$ , in the pre and post disaster change images respectively.  $\bar{t}_{\alpha}^1, s_{t_{\alpha}^1}$  are the mean and the standard deviation of class  $\alpha$  in the pre-disaster change image respectively. Prior to the validation of the results, thresholds were applied to change maps in order to segment the pixels into the changed and the unchanged classes. The thresholds were determined by investigating the pixel distribution in the regions under change. Resulting threshold values for each filtered and texture images are reported in Table 1. Finally these segmented maps were converted to fractional maps with respect to the changed (damaged area) pixels. This fractional estimation was carried out using a 5×5 pixel window.

**Table 1:** Threshold values to extract the damage and non-damage classes.

Image	Polarization	Threshold Value
Noise variance ( $\sigma_u^2$ )	HH	0.102
	HV	0.075
	VH	0.081
	VV	0.104
Weight ( $\theta$ )	HH	0.302
	HV	0.246
	VH	0.247
	VV	0.287
Normalized Ratio	HH	1.100
	HV	1.067
	VH	1.069
	VV	1.103
PCA		2.202
Adaptive Lee filter	HH	0.064
	HV	0.070
	VH	0.071
	VV	0.068



## 4 Experimental Results

Generation of MAR texture images, as well as the variograms, SSIM and MRD analysis were carried out using R programming environment, version 3.0.1 (R 3.0.1). The influence of the disaster on the urban spatial structure represented in both adaptive Lee filtered and the MAR based texture images were examined using the variograms. Interestingly, they show important differences in both these cases. A 50×200 pixel transect in the urban region running from west to east for both lag distance and radius of 10 pixels, was used to generate the variograms. Variogram matrices and the Variogram plots for Lee filtered HH and HV, log HH and HV with their texture components,  $\theta$  and  $\sigma_u^2$  are shown in Fig. 7. Transect generated over the urban area consists of well-developed city features, including planned housing networks, roads, railways and canals. It was also observed using the Google earth pre and post disaster images that the tsunami damages are significant along the coast. This balanced city structure was heavily influenced by the tsunami and earth quake. In the case of variograms generated for the filtered images (Fig.7 top 4 plots), the heights of the variograms stayed close to each other. It can be seen from the results that the variograms begin with relatively low values but did not level within the considered lag distance of 10 pixels. Furthermore, in all these cases, the variogram shape was similar to a spherical mode. The gradual slope common to the filtered variograms shows a higher variance in the size of the objects. Hence the variograms generated for the filtered images failed to convey any significant changes in the density of objects such as buildings, size of objects in the scene or the variance in the size of the objects. The main difference of the pre and post disaster variograms for the MAR based texture is that in the pre disaster situation, the shape of the variograms is close to a spherical model, while in the case of the post disaster it is almost an exponential model. The exponential model never reaches the sill but asymptotically approaches it. The sharp rise to the sill represents a considerable variance in the size of the urban features due to the effect of the disaster. The anisotropic variance shown by the variogram matrices for the lognormal images, as well as the MAR based texture images ( $\theta$ ,  $\sigma$ ), further justifies the change in variance of the objects after the disaster. This could happen due to the rubble and the significant destruction to the planned arrangement of urban objects caused by the tsunami effect. Additionally, the change in the sill relates to the change in object density due to the impact of the disaster along the area of transect. Variograms calculated using MAR based texture values shows the regions undergoing spatial variations due to the disaster. While in the filter based approaches, the higher variance in the object sizes stays same for both the pre and post disaster SAR images, making it difficult to identify important changes.

The SSIM maps generated from the pre and post disaster speckle filtered and texture images are shown in Fig.8. The use of SSIM to study the structural similarity between images is not feasible without the speckle filtering, because any random noise can significantly change the mean luminance and the contrast. However, with MAR models,

the multiplicative effect of the speckle is subtracted in a local neighborhood. With the treatment of noise in this respect, it is possible to use image quality measure, such as SSIM, for the temporal change determination. The local statistics  $\mu$ ,  $\sigma$  for the SSIM index in Eq. 14 were calculated using a 3×3 local window to generate the SSIM index maps. Visually the images show that the SSIM on filtered images (Fig. 8 (a), (b), (c), (d)) were not fully capable to discriminate the changes, but low SSIM values resulted in the regions subjected to changes. On the contrary, SSIM perform well to discriminate changes and non-changes using MAR based texture images.

Visually the SSIM maps suggest that the coastal area has been affected with significant structural changes, with darker shades in the MAR based texture. Further, the significant damages surrounding the Kitakami River due to inland tsunami effects along the river basin are well represented. The cross polarized texture measures (Fig 8 (f), (g), (j), (k)) show low sensitivity to the changes, with respect to the co-polarized texture.

**Table 2:** SSIM measures for the change images.

Pre and post disaster images	Average SSIM
Adaptive Lee filtered intensity HH	0.5136
Adaptive Lee filtered intensity HV	0.5160
Adaptive Lee filtered intensity VH	0.5179
Adaptive Lee filtered intensity VV	0.5112
MAR based Weight HH	0.9854
MAR based Weight HV	0.9845
MAR based Weight VH	0.9849
MAR based Weight VV	0.9852
MAR based Variance HH	0.9998
MAR based Variance HV	1.0000
MAR based Variance VH	1.0000
MAR based Variance VV	0.9988

The reported SSIM values for the pre and post disaster despeckled and texture images are shown in Table 2. SSIM values stayed in the range 0.98 to 1.0 for the MAR based texture. It drops to the range of 0.5 for the filtered images. This suggests the average performance in discriminating changes using the adaptive filters. It also means that the SSIM encountered significant random noise, even after filter operations, while determining the structural similarity between the pre and post disaster pixels. Modelling the spatial correlation before the change analysis using MAR models can be effective to reduce this random noise, especially for the SAR data.

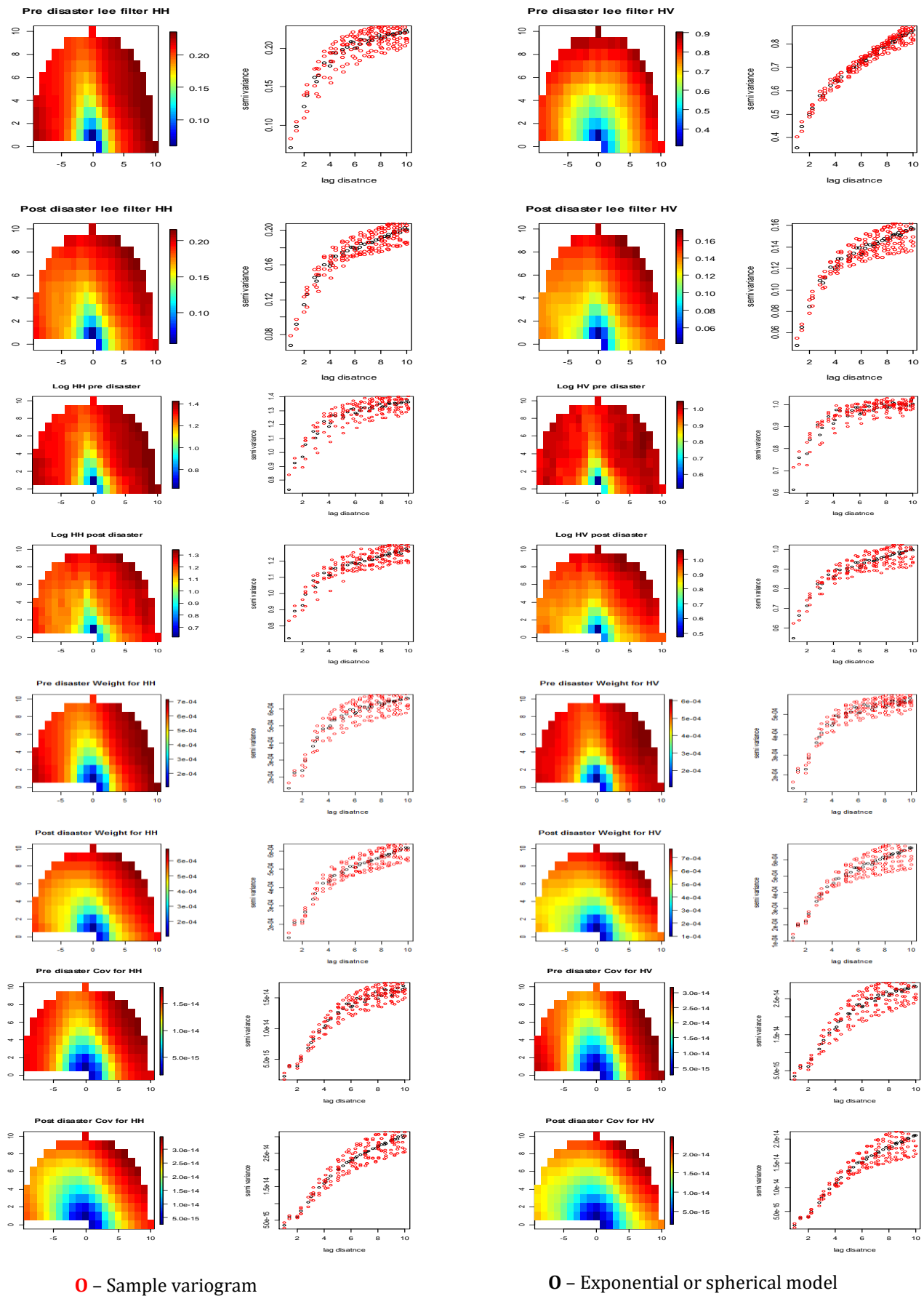


**Fig. 7:** Variogram matrices and the Variogram plots for log HH, HV components and their texture components,  $\theta$  and  $\sigma_u^2$  respectively, along a transect over the urban area before the disaster and after, showing the change of the variograms shape from spherical to exponential. And the matrices show the isotropic variance with respect to lag distance corresponding to the variogram.

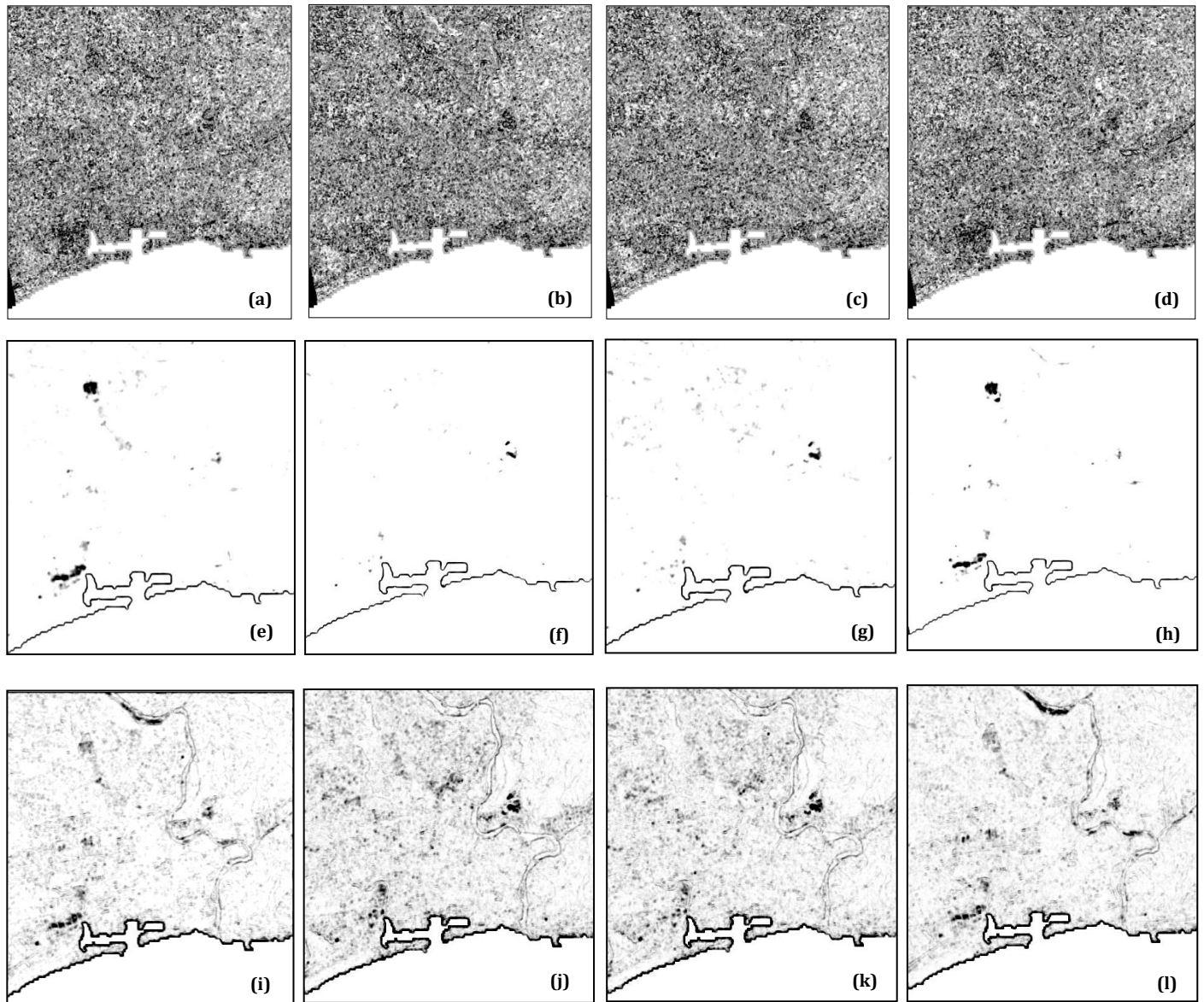
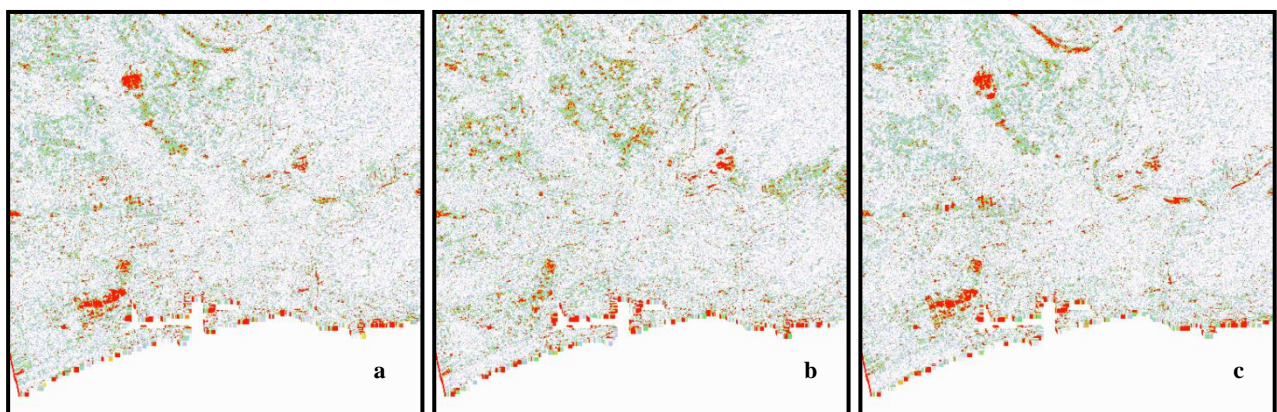


**Fig. 8:** SSIM maps with brightness indicating the magnitude of the local structural similarity, the darker areas clearly relates to the changes (a), (b), (c), (d) SSIM between pre and post disaster log transformed filtered intensity images (e), (f), (g), (h) SSIM between pre and post disaster  $\sigma_u^2$  (i), (j), (k), (l) SSIM between pre and post disaster  $\theta$  of HH, HV, VH, VV polarization respectively. SSIM shows improved discrimination between change and no change areas using the texture measure.



**Damage intensity from low to high**

**Fig. 9:** Change maps using MRD for log transformed filtered intensity images (a) (b) (c), HH, HV, VV polarization, respectively.



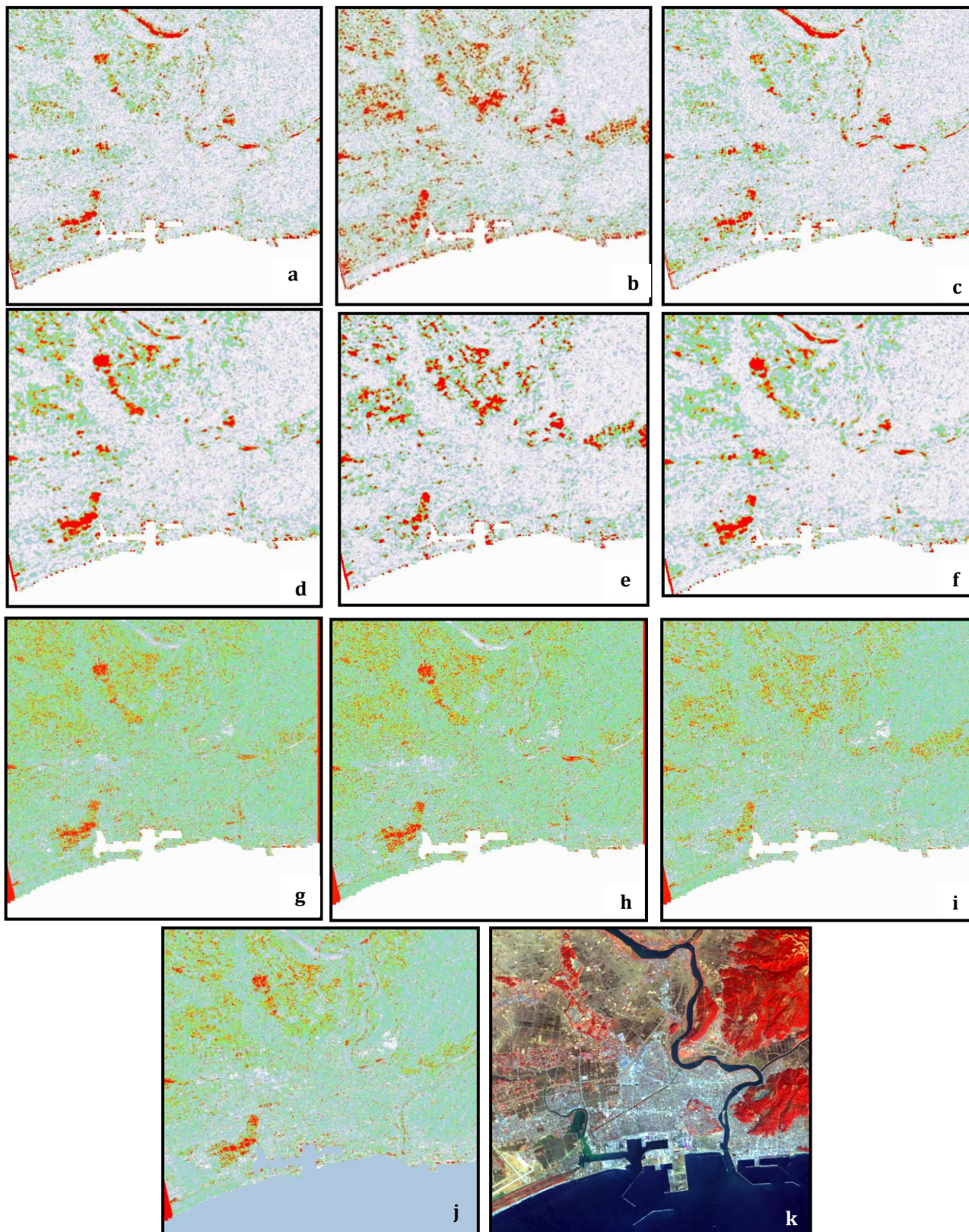


**Fig. 10:** Change maps using MRD for MAR model based texture formed by using  $\theta$  vector for HH, HV, VV (a) (b) (c), MAR model texture formed by using  $\sigma_u^2$  for HH, HV and VV polarization, (d), (e), (f), Mean ratio based change estimate using log estimates of SAR intensity for HH, HV and VV, using the second PCA component of the pre and post disaster log estimates of HH, HV, VH and VV components, (g, h, i, j) and the post disaster AVNIR-2 image showing the major land cover components for the same study region (k), High level of damages are shown in red colour.

Finally in the case of MRD, we analysed the results with respect to the PCA and ratio based temporal changes as well as the adaptive filter based changes. The change results based on MRD are shown in Fig. 9 and Fig.10.

Ground truth information for the samples was obtained by interpreting a post disaster advanced AVNIR-2 and Google earth pre and post disaster images. Visual interpretation of the results for each technique suggests that the MAR based texture parameters extracted the coastal area damages, flooded paddy lands and the damages along the river borders with better contextual smoothing. According to Fig. 10, all the three techniques resulted in a common disaster signature along the coastal impervious land cover, paddy lands, along the river and to the north part of the river due to tsunami flooding and earthquake. The right part of the town was not exposed to the tsunami as much as the left part. This is mainly because (full SAR image Fig.1) the right part is protected by the expanding bay area and the higher elevation forest area. Hence the inundations in the left part and the middle of the town are not common to the right part. The MRD results using the filtered images as a whole show change closely and in-line with the texture based results. Nevertheless, despekeled image changes can be seen as a mixture of change pixels and the pixels representing noise. Earlier, the noise effect with the filter images was also experienced in the variogram and the SSIM based change results. This is clearly evident along the coast as well as along the river basins (Fig. 9 left bottom and right upper regions). Context based change detection results using MAR model parameters, have managed to accounted for small scale variations of damages by

separating them from noise, with significantly low salt and pepper effects.

According to the error measures (Table 3 and 4), structural changes estimated using MAR texture measures based on the neighborhood weighting parameter vector and the noise variance have very high correlation in the range of 0.8, with least AEP and RMSE in the range of 0.004 and 0.06 for the co-polarized SAR images. Higher correlation between the textures ( $\theta, \sigma_u^2$ ) based change results can be seen for all the polarization components. The comparison also suggests that the MAR texture based changes for the co-polarized components have considerably better agreement with PCA based approach than the normalized log ratio based approach with better average AEP of 0.003, RMSE 0.06 and CC of 0.74. The same results have been followed by the cross polarized components, but with lower accuracy levels. The CC measures between the MAR and adaptive filter based changes show significantly high correlation in the range of 0.97 to 0.99 for both cross and co-polarized SAR images. Yet, significant differences between them were suggested by the higher AEP and RMSE values in the range of 0.01 to 0.3 and 0.1 to 0.3 for co and cross polarized results, respectively. It is difficult to say from this which result is superior. Yet it shows that the changes resulting from MAR based texture are different to the changes coming out from ordinary noise filtered images. The results in total show that the MRD based MAR texture approach for temporal changes produce more generalized and smoother outputs, while having better fractional agreement with PCA based approaches.

**Table 3:** Error measures between co-polarized components.

Cross comparison combinations (co-polarized input) change images	AEP	RMSE	CC
MAR based Variance (HH) vs. Lee filtered (HH)	0.029	0.081	0.997
MAR based Variance (VV) vs. Lee filtered (VV)	0.026	0.080	0.997
MAR based Weight (HH) vs. Lee filtered (HH)	0.207	0.300	0.977
MAR based Variance (VV) vs. Lee filtered (VV)	0.210	0.305	0.976
MAR based Variance (HH) vs. MAR based Weight (HH)	0.004	0.059	0.865
MAR based Variance (VV) vs. MAR based Weight (VV)	0.005	0.068	0.824
MAR based Variance (HH) vs. PCA2	0.002	0.074	0.778
MAR based Variance (VV) vs. PCA2	0.001	0.076	0.780
MAR based Weight (HH) vs. PCA2	0.006	0.063	0.717
MAR based Weight (VV) vs. PCA2	0.005	0.062	0.710
MAR based Variance (HH) vs. Log Ratio (HH)	0.017	0.076	0.769
MAR based Variance (VV) vs. Log Ratio (HH)	0.015	0.080	0.758
MAR based Variance (HH) vs. Log Ratio (VV)	0.016	0.080	0.737
MAR based Variance (VV) vs. Log Ratio (VV)	0.014	0.077	0.765
MAR based Weight (HH) vs. Log Ratio (HH)	0.022	0.075	0.682
MAR based Weight (VV) vs. Log Ratio (HH)	0.021	0.077	0.645
MAR based Weight (HH) vs. Log Ratio (VV)	0.021	0.078	0.656



MAR based Weight (VV) vs. Log Ratio (VV)	0.019	0.076	0.654
Log Ratio (HH) vs. PCA2	0.014	0.046	0.881
Log Ratio (VV) vs. PCA2	0.013	0.045	0.885

**Table 4:** Error measures between cross-polarized components.

Cross comparison combinations (cross-polarized input) change images	AEP	RMSE	CC
MAR based Variance (HV) vs. Lee filtered (HV)	0.018	0.064	0.997
MAR based Variance (VH) vs. Lee filtered (VH)	0.021	0.069	0.998
MAR based Weight (HV) vs. Lee filtered (HV)	0.032	0.106	0.994
MAR based Weight (VH) vs. Lee filtered (VH)	0.016	0.058	0.996
MAR based Variance (HV) vs. Mar Based Weight (HV)	0.009	0.062	0.865
MAR based Variance (VH) vs. MAR based Weight (VH)	0.018	0.071	0.800
MAR based Variance (HV) vs. PCA2	0.008	0.102	0.520
MAR based Variance (VH) vs. PCA2	0.001	0.090	0.485
MAR based Weight (HV) vs. PCA2	0.017	0.106	0.466
MAR based Weight (VH) vs. PCA2	0.016	0.107	0.434
MAR based Variance (HV) vs. Log Ratio (HV)	0.014	0.104	0.517
MAR based Variance (VH) vs. Log Ratio (VH)	0.022	0.092	0.497
MAR based Weight (HV) vs. Log Ratio (HV)	0.023	0.105	0.494
MAR based Weight (VH) vs. Log Ratio (VH)	0.023	0.107	0.416
Log Ratio (HV) vs. PCA2	0.006	0.058	0.654
Log Ratio (VH) vs. PCA2	0.021	0.064	0.681

## 5 Conclusion and Discussion

MAR model parameters, since their introduction, have been used successfully with Markov Random Field base classification mechanisms for better contextual smooth classification outputs from multisource data. Yet their capabilities in time series data analysis, especially to detect contextual changes in land cover, have not been investigated fully. In this regard, the main goal of this work was to investigate the performance of MAR texture measures of SAR data, to extract contextual changes resulting from disasters. The study proposed the use of MAR based texture for time series SAR data change analysis independent of polarimetric approaches. Affected area of the Tohoku, earthquake and tsunami in the year 2011 off the pacific coast of Japan, was chosen as the study site. Three different techniques to detect the structural changes using MAR based texture measure were presented in this study. A significant finding of the study was the changes in the shape and height of the variograms from spherical to exponential, depending on the damages to the structure. Hence, the extensive use of variograms with MAR base texture at different transects over the study region can predict the areas exposed to major changes. The noise free

setup of the MAR based texture provides the feasibility to use the SSIM for the study. The change areas always represented the dissimilarity between the pre and the post disaster scenes. The temporal changes extracted from the SSIM based analysis corresponds similarly to the change detection results of the MRD. Finally, MRD extracts the change pixels from the non-change one. The visual inspection showed that the MAR texture parameters were more sensitive to the small scale variations of the change. Noise free results with better smoothing can be observed in the MAR texture, comparative to the PCA and normalized ratio based approaches. It can be useful to apply the technique for different disaster situations with proper ground truth information for further evaluation. MAR based SAR texture preserves the original SAR information and provides a better discrimination for the changed and no changes classes.

### Acknowledgement

Authors acknowledge the resources provided by the Department of Civil and Earth Resources Engineering, Kyoto University, in order to succeed in this research work.

## Author Contributions

Conceptualization, methodology, analysis, writing—original draft preparation, D.R.W., and writing—review and editing, T.M.. All authors have read and agreed to the published version of the manuscript.

## Conflict of Interest

The authors declare no conflict of interest.

## References

- Bruzzone, L., Prieto, D. F., 2000. Automatic analysis of the difference image for unsupervised change detection. *IEEE Transactions on Geoscience and Remote sensing*. 38, 1171-1182.
- Bujor, F., Trouvé, E., Valet, L., Nicolas, J.-M., Rudant, J.-P., 2004. Application of log-cumulants to the detection of spatiotemporal discontinuities in multitemporal SAR images. *IEEE Transactions on Geoscience and Remote Sensing*. 42, 2073-2084.
- Chellappa, R., Chatterjee, S., 1985. Classification of textures using Gaussian Markov random fields. *IEEE Transactions on Acoustics, Speech, and Signal Processing*. 33, 959-963.
- Cross, G. R., Jain, A. K., 1983. Markov random field texture models. *IEEE Transactions on Pattern Analysis and Machine Intelligence*. 25-39.
- Curran, P. J., 1988. The semivariogram in remote sensing: an introduction. *Remote sensing of Environment*. 24, 493-507.
- Dekker, R. J., 2003. Texture analysis and classification of ERS SAR images for map updating of urban areas in the Netherlands. *IEEE Transactions on Geoscience and Remote Sensing*. 41, 1950-1958.
- Del Frate, F., Pacifici, F., Solimini, D., 2008. Monitoring urban land cover in Rome, Italy, and its changes by single-polarization multitemporal SAR images. *IEEE Journal of Selected Topics in Applied Earth Observations and Remote Sensing*. 1, 87-97.
- Dierking, W., Skriver, H., 2002. Change detection for thematic mapping by means of airborne multitemporal polarimetric SAR imagery. *IEEE Transactions on Geoscience and Remote Sensing*. 40, 618-636.
- Ehrlich, D., Guo, H., Molch, K., Ma, J., Pesaresi, M., 2009. Identifying damage caused by the 2008 Wenchuan earthquake from VHR remote sensing data. *International Journal of Digital Earth*. 2, 309-326.
- Frankot, R. T., Chellappa, R., 1987. Lognormal random-field models and their applications to radar image synthesis. *IEEE Transactions on Geoscience and Remote Sensing*. 195-207.
- Gamba, P., Aldrighi, M., 2012. SAR data classification of urban areas by means of segmentation techniques and ancillary optical data. *IEEE Journal of Selected Topics in Applied Earth Observations and Remote Sensing*. 5, 1140-1148.
- Gamba, P., Dell'Acqua, F., Lisini, G., 2006. Change detection of multitemporal SAR data in urban areas combining feature-based and pixel-based techniques. *IEEE Transactions on Geoscience and Remote Sensing*. 44, 2820-2827.
- Haralick, R. M., Shanmugam, K., Dinstein, I. H., 1973. Textural features for image classification. *IEEE Transactions on systems, man, and cybernetics*. 610-621.
- Inglada, J., Mercier, G., 2007. A new statistical similarity measure for change detection in multitemporal SAR images and its extension to multiscale change analysis. *IEEE transactions on geoscience and remote sensing*. 45, 1432-1445.
- Liu, Y., Nishiyama, S., Yano, T., 2004. Analysis of four change detection algorithms in bi-temporal space with a case study. *International Journal of Remote Sensing*. 25, 2121-2139.
- Mather, P., Tso, B., 2016. Classification methods for remotely sensed data. CRC press.
- Ord, K., 1975. Estimation methods for models of spatial interaction. *Journal of the American Statistical Association*. 70, 120-126.
- Park, S., Lee, T., Hong, S., Moon, W., Investigation of April 2000 forest fire in Kang-won province, Korea using RADARSAT data, paper presented at In Geoscience and Remote Sensing Symposium. IGARSS, 2001.
- Qiu, F., Berglund, J., Jensen, J. R., Thakkar, P., Ren, D., 2004. Speckle noise reduction in SAR imagery using a local adaptive median filter. *GIScience & Remote Sensing*. 41, 244-266.
- Richards, J. A., 2009. Remote sensing with imaging radar. Springer.
- Singh, A., 1990. Digital change detection techniques using remotely-sensed data 1989. *Int. J. Remote Sensing*. 10, 989-100.
- Solberg, A. S., Jain, A. K., 1997. Texture fusion and feature selection applied to SAR imagery. *IEEE Transactions on Geoscience and Remote Sensing*. 35, 475-479.
- Stasolla, M., Gamba, P., 2008. Spatial indexes for the extraction of formal and informal human settlements from high-resolution SAR images. *IEEE Journal of Selected Topics in Applied Earth Observations and Remote Sensing*. 1, 98-106.
- The R Project for Statistical Computing, edited. <http://www.r-project.org/>, accessed 2021.03.04
- Ulaby, F. T., Kouyate, F., Brisco, B., Williams, T. L., 1986. Textural information in SAR images. *IEEE Transactions on Geoscience and Remote Sensing*. 235-245.
- Wang, Z., Bovik, A. C., Sheikh, H. R., Simoncelli, E. P., 2004. Image quality assessment: from error visibility to structural similarity. *IEEE transactions on image processing*. 13, 600-612.
- Woodcock, C. E., Strahler, A. H., Jupp, D. L., 1988. The use of variograms in remote sensing: I. Scene models and simulated images. *Remote Sensing of Environment*. 25, 323-348.